

ARTICLE

Received 31 Jul 2015 | Accepted 19 Oct 2015 | Published 18 Nov 2015

DOI: 10.1038/ncomms9932

OPEN

Low-temperature-processed efficient semi-transparent planar perovskite solar cells for bifacial and tandem applications

Fan Fu¹, Thomas Feuerer¹, Timo Jäger¹, Enrico Avancini¹, Benjamin Bissig¹, Songhak Yoon², Stephan Buecheler¹ & Ayodhya N. Tiwari¹

Semi-transparent perovskite solar cells are highly attractive for a wide range of applications, such as bifacial and tandem solar cells; however, the power conversion efficiency of semi-transparent devices still lags behind due to missing suitable transparent rear electrode or deposition process. Here we report a low-temperature process for efficient semi-transparent planar perovskite solar cells. A hybrid thermal evaporation–spin coating technique is developed to allow the introduction of PCBM in regular device configuration, which facilitates the growth of high-quality absorber, resulting in hysteresis-free devices. We employ high-mobility hydrogenated indium oxide as transparent rear electrode by room-temperature radio-frequency magnetron sputtering, yielding a semi-transparent solar cell with steady-state efficiency of 14.2% along with 72% average transmittance in the near-infrared region. With such semi-transparent devices, we show a substantial power enhancement when operating as bifacial solar cell, and in combination with low-bandgap copper indium gallium diselenide we further demonstrate 20.5% efficiency in four-terminal tandem configuration.

¹Laboratory for Thin Films and Photovoltaics, Empa—Swiss Federal Laboratories for Materials Science and Technology, Ueberlandstrasse 129, 8600 Dübendorf, Switzerland. ²Laboratory for High Performance Ceramics, Empa—Swiss Federal Laboratories for Materials Science and Technology, Ueberlandstrasse 129, 8600 Dübendorf, Switzerland. Correspondence and requests for materials should be addressed to F.F. (email: Fan.Fu@empa.ch) or to S.B. (email: Stephan.Buecheler@empa.ch).

The emerging perovskite solar cells have received increasing attention due to the high efficiency, easy processing and potentially low cost^{1–2}. Although the power conversion efficiency of perovskite solar cells have soared up to 20.1% (ref. 3), there is still ample room for further efficiency improvement through novel concepts^{4–6}. An effective approach to increase the efficiency and lower the production cost is to make semi-transparent solar cells that can convert solar energy into electricity from both front and rear side of the device⁷. The bifacial cell concept has been implemented in various kinds of solar cell technologies^{8–12}, and up to 50% output power enhancement has been demonstrated in Si wafer bifacial modules by collecting the albedo radiation from surroundings¹³. In addition, the semi-transparent perovskite solar cells hold great promise for applications in tandem solar cells¹⁴, photon energy upconversion¹⁵, building-integrated photovoltaics¹⁶, wearable electronics¹⁷, powering sensors and electronic gadgets in homes.

There are still many challenges hindering the realization of high-performance semi-transparent perovskite solar cells. The state-of-the-art perovskite solar cells^{3,18–22} employ high-temperature-processed ($\sim 500^\circ\text{C}$) TiO_2 (mesoporous and compact) as electron transporting layer (ETL), which is incompatible with monolithic tandem or flexible solar cells on plastics. Thus, it is desirable to develop a planar structure that allows low-temperature processing. It is well known that perovskite solar cells, particularly in planar configuration with TiO_2 as ETL, suffer from pronounced hysteresis in the current density–voltage (J – V) curve, which often results in overestimated device performance²³. Therefore, it is imperative to eliminate the hysteresis, which is not only important to ensure a stable performance but also to unambiguously evaluate the real device efficiency. [6,6]-phenyl- C_{61} -butyric acid methyl ester (PCBM) has been proven to assist in eliminating the J – V hysteresis in inverted device configuration²⁴. Several efforts have been made in positioning PCBM in regular device structure; however, the hysteresis phenomenon still remains^{25,26}. For bifacial and tandem solar cell applications, it is crucial to replace the commonly used metal contacts in perovskite cells by highly transparent conducting electrodes, which allow sunlight incident from front and rear side of the device and to transmit the photons with energy below the bandgap of the perovskite. Previously, thin layers of Au (ref. 27),

carbon nanotubes²⁸ and PEDOT:PSS²⁹ have been explored as transparent contact for perovskite solar cells, while the efficiencies are generally below 10% and these contacts featured strong absorption in near infrared (NIR). Efficient semi-transparent devices have been realized with graphene rear electrode; however, all the devices show strong hysteresis in current density–voltage curves^{30,31}. Recently, sputtered transparent conductive oxides (TCO), including indium tin oxide (ITO)³², ZnO:Al ³³ and indium zinc oxide (IZO)³⁴, have been reported with highest efficiency of up to 12.1% for a semi-transparent cell and 19.5% in perovskite–CIGS (copper indium gallium diselenide) four-terminal configuration³³. Bailie *et al.*³⁵ developed a 12.7% efficiency semi-transparent perovskite solar cell employing Ag nanowires, and demonstrated 18.6 and 17% tandem efficiency by combining with CIGS and low-quality silicon bottom cell, respectively. Despite the high NIR transparency and low sheet resistance of Ag nanowires, the complicated deposition method leads to large efficiency variation and poor reproducibility, and the fast diffusion of Ag into Spiro-OMeTAD and perovskite results in degradation of device stability and performance³⁶. Therefore, the implementation of a suitable transparent electrode material and deposition process is the key and challenge to high-efficiency semi-transparent perovskite solar cells. An ideal transparent electrode for perovskite solar cells should meet the following requirements: superior transparency in visible and NIR region, low sheet resistance, robust adhesion, good chemical stability and compatibility with adjoining layers. As the perovskite and Spiro-OMeTAD are temperature and solvent sensitive³⁵, a low-temperature and dry process would be favoured for the deposition of transparent electrodes. In this regard, the room-temperature sputtering deposited TCO would be an ideal candidate.

Here we report a low-temperature ($\leq 50^\circ\text{C}$)-processed hysteresis-free high-efficiency semi-transparent planar perovskite solar cell. The hysteresis is eliminated through a PCBM interlayer and high-quality perovskite absorber enabled by the hybrid thermal evaporation–spin coating method. High-mobility hydrogenated indium oxide ($\text{In}_2\text{O}_3:\text{H}$) is employed as transparent rear electrode through a room-temperature radio-frequency magnetron sputtering, which enables a semi-transparent device with steady-state efficiency of 14.2% and 72% average

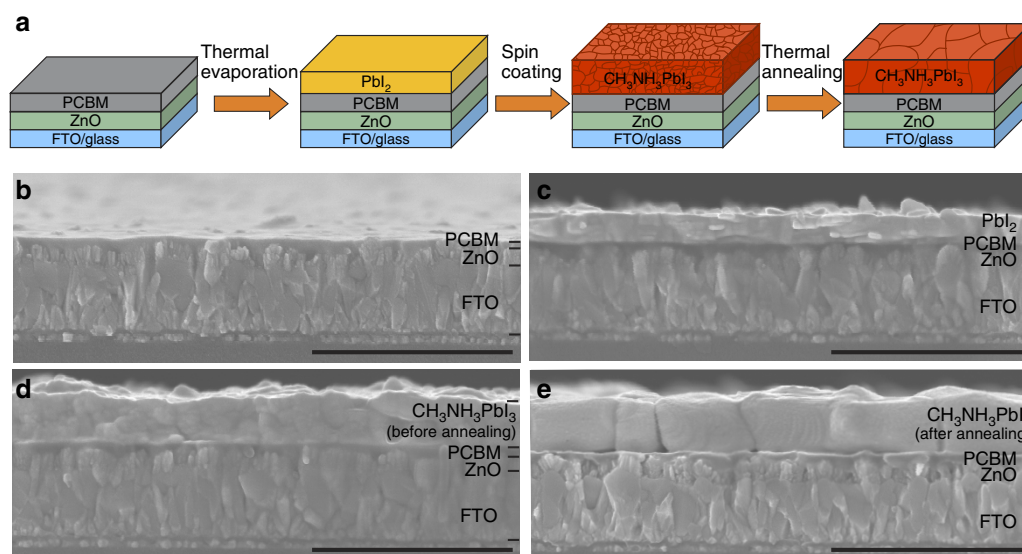


Figure 1 | Hybrid thermal evaporation–spin coating preparation method and corresponding microstructure. (a) Deposition of perovskite layer through a combined thermal evaporation of PbI_2 and spin coating of CH_3NH_3 solution in isopropanol followed by 2 h annealing at 50°C on hotplate. (b–e) The cross-sectional SEM images of each layer during perovskite preparation. Scale bars, 1 μm in b–e.

transmittance between 800 and 1,150 nm. Such a device when operated as a bifacial cell yields an additional 13.5% power output improvement, and 20.5% efficiency is demonstrated using perovskite top cell and CIGS bottom cell in four-terminal tandem configuration.

Results

Low-temperature-processed planar perovskite solar cells.

Figure 1 shows a schematic drawing and cross-sectional scanning electron microscopy (SEM) images of the perovskite absorber deposited by hybrid thermal evaporation–spin coating method. The high-temperature-processed TiO_2 is replaced by ~ 100 nm compact ZnO layer deposited through radio-frequency magnetron sputtering at room temperature, followed by spin coating of ~ 50 nm PCBM. The room-temperature-processed ETL is attractive for low-cost, lightweight and flexible plastic substrates, and compatible with monolithic tandem fabrication. As illustrated in Fig. 1a, the perovskite layer is formed through a

hybrid evaporation solution approach, where a compact PbI_2 layer is initially deposited by thermal evaporation³⁷. This method allows a uniform and compact PbI_2 deposited over large area. Then $\text{CH}_3\text{NH}_3\text{I}$ in isopropanol solution is added by spin coating, followed by thermal annealing at 50°C for 2 h on hotplate. Afterwards, ~ 200 nm Spiro-OMeTAD is spin coated on top of the perovskite. Finally, the cell is finished by evaporating 60 nm Au for opaque reference solar cells. For semi-transparent solar cells, thermally evaporated MoO_3 and room-temperature-sputtered $\text{In}_2\text{O}_3:\text{H}$ are employed as rear contact. Thus, the highest processing temperature during the opaque and semi-transparent device fabrication is not higher than 50°C . More detailed fabrication process information can be found in the Methods section.

For planar perovskite solar cells, a uniform and compact perovskite layer is essential for achieving high efficiency³⁸. As ZnO conformally covers the rough fluorine-doped tin oxide (FTO) surface, the deposition of PCBM smoothens the surface where the perovskite is grown (Fig. 1b). Consequently, the

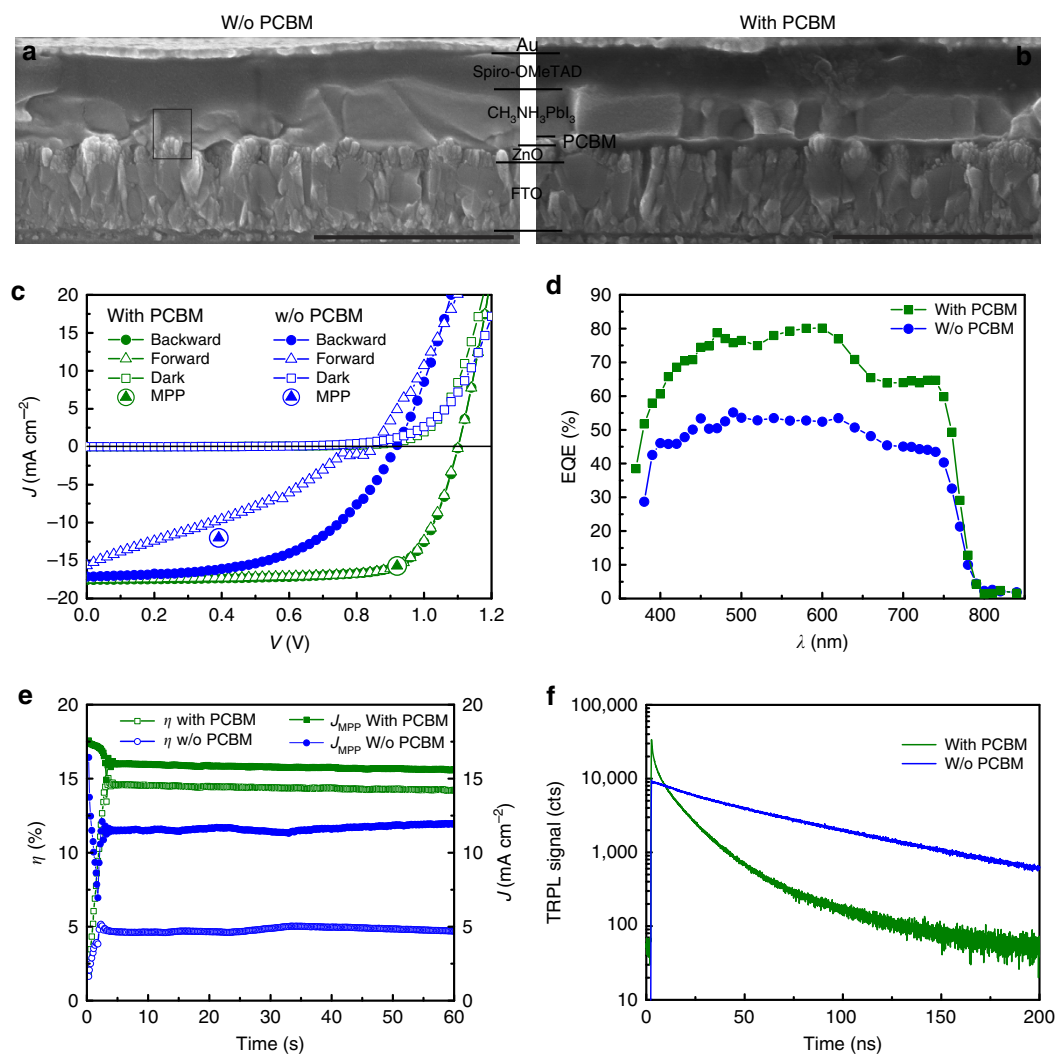


Figure 2 | Microstructure, time-resolved photoluminescence and photovoltaic performance of planar perovskite solar cells. (a,b) The cross-sectional SEM images of devices without (a) and with (b) PCBM, respectively. The rectangular area in a indicates shunting path. (c–e) The current density–voltage (J – V) curves (c), EQE spectra (d) and steady-state efficiency at maximum power point (e) of the planar perovskite solar cells. All the devices are measured under simulated AM1.5G irradiation with $1,000 \text{ W m}^{-2}$ intensity. The J – V measurements are performed in both forward (-0.1 to 1.2 V) and backward (1.2 to -0.1 V) direction at a scan rate and delay time of 0.3 V s^{-1} and 10 ms , respectively. The steady-state efficiency is evaluated by using a maximum power point tracker algorithm with constant AM1.5G illumination. (f) Time-resolved photoluminescence for samples with and without PCBM layer. Scale bars, $1 \mu\text{m}$ in a and b. W/o, without.

thermally evaporated PbI_2 exhibits a compact and uniform layer over large area (Fig. 1c). Figure 1d,e presents the cross-sectional SEM images of perovskite layer before and after annealing, showing that the perovskite layer retained the desired compact morphology from parent PbI_2 . With thermal annealing, the grain size increases considerably from several tens of nanometres to values comparable to the film thickness (Fig. 1d,e), which might be beneficial to the transport and recombination properties of the absorber.

The herein introduced perovskite preparation method offers several merits. In previously reported two-step methods where PbI_2 is spin coated from solution, it is quite challenging to control the morphology of the PbI_2 film deposited from solution on planar substrates³⁹. The low solubility of PbI_2 in the commonly used solvent *N,N*-dimethylformide⁴⁰ could limit the thickness variation and the choice of the underlying substrates where PbI_2 is deposited. We overcome these challenges by using a simple thermal evaporation method, which can deposit a compact and uniform PbI_2 layer with precisely controlled thickness over large area. The room-temperature vapour deposition has no constraints on the underlying substrates, which opens up numerous possibilities for exploring other solvent-sensitive carrier-selective contacts and novel cell structure. For instance, this process allows the introduction of PCBM below the perovskite layer, which is crucial to eliminate the J - V hysteresis²⁴, but difficult to realize in solution process as the commonly used polar solvents, such as *N,N*-dimethylformide, dimethylsulfoxide or γ -butyrolactone, for perovskite formation are detrimental to thin layers of PCBM.

Planar perovskite solar cells without J - V hysteresis. The hybrid thermal evaporation–spin coating method enables us to investigate the influences of PCBM on perovskite microstructure and device performance in regular planar configuration. Figure 2a,b presents the cross-sectional SEM images of the planar perovskite solar cell with and without PCBM layer, respectively. Other than PCBM, the devices are fabricated by an identical process with perovskite layer grown from 120 nm PbI_2 (estimated by quartz microbalance) and 40 mg ml⁻¹ $\text{CH}_3\text{NH}_3\text{I}$ solution. It can be seen from the SEM images that the perovskite layer shows considerable surface roughness and thickness non-uniformity when grown directly on ZnO, which leads to low-resistance shunting paths and insufficient light absorption. A uniform and compact perovskite layer with large grain size is obtained when grown on PCBM. The microstructural difference in perovskite layers is mainly attributed to the morphological differences in PbI_2 layers, as shown in Supplementary Fig. 1. If PbI_2 is grown on ZnO directly, porous layers comprising numerous nanoplates are obtained⁴¹. This could form lots of grain boundaries and defects after the conversion into perovskite. It is important to note that high-efficiency devices produced by the here described process always contain residual PbI_2 as shown in Supplementary Fig. 2. The existence of residual PbI_2 is also observed in many high-efficiency devices reported in literature and several beneficial effects, for example, grain boundary passivation, hole-blocking effect and so on, have been proposed^{42,43}.

Figure 2c shows the J - V characteristics of the corresponding planar perovskite solar cells under simulated AM1.5G irradiation. Owing to the hysteresis in J - V measurements³¹, it is crucial to report both forward (short circuit to forward bias) and backward (forward bias to short circuit) measurements along with the measurement conditions. The photovoltaic parameters are summarized in Supplementary Table 1. The device with PCBM layer shows an open circuit voltage (V_{oc}) of 1.101 V, short circuit current density (J_{sc}) of 17.6 mA cm⁻² and fill factor (FF) of

74.9%, resulting in power conversion efficiency (η) of 14.5% in forward scan. In backward scan a V_{oc} of 1.103 V, J_{sc} of 17.5 mA cm⁻², FF of 74.6% and η of 14.4% are obtained. The J - V curves from forward and backward scans coincide well, indicating no J - V hysteresis is observed in the devices. The J_{sc} is confirmed by external quantum efficiency (EQE) measurement (Fig. 2d) with an integrated J_{sc} of 17.4 mA cm⁻² under AM1.5G spectrum. Furthermore, the efficiency measured at the maximum power point (MPP), that is, the steady-state output of the device, is shown in Fig. 2e. The cell exhibits a steady-state efficiency of 14.4% and current density of 15.7 mA cm⁻² at MPP under continuous illumination. This is consistent with the J - V and EQE measurements. The device without PCBM layer generally shows a lower V_{oc} , J_{sc} and FF with pronounced J - V hysteresis, and the steady-state efficiency lies between forward and backward efficiency. The integrated J_{sc} of 12.1 mA cm⁻² is also lower than that derived from the J - V measurement.

Time-resolved photoluminescence decays are presented in Fig. 2f to probe the effect of PCBM on carrier dynamics in perovskite solar cells. In both cases the decay tails allow to estimate a minority carrier lifetime of ~ 80 ns (ref. 44). Furthermore, it can be seen that the addition of PCBM leads to a nonlinear initial PL transient, which can be explained by charge-separating fields⁴⁵. This indicates that the application of PCBM promotes a working junction without the need of initial biasing. Therefore, the elimination of J - V hysteresis and enhanced photovoltaic performance primarily stem from improved interface and junction formation and from the high-quality perovskite layer with enhanced crystallinity, uniform and compact morphology with large grain size.

Semi-transparent planar perovskite solar cells. For semi-transparent cells, the opaque Au is substituted by $\text{In}_2\text{O}_3:\text{H}$ transparent electrodes. $\text{In}_2\text{O}_3:\text{H}$ is a high-mobility TCO material with superior visible and NIR transmittance⁴⁶, and excellent thermal and chemical stability for solar cell applications were reported⁴⁷. Deposition of $\text{In}_2\text{O}_3:\text{H}$ by sputtering at room temperature without post-annealing results in layers with reasonably high mobility of 51.3 cm² V⁻¹ s⁻¹ and sheet resistance of 25.7 Ω per square for 149 nm thick (determined from profilometer) amorphous layers. The effect of post-annealing treatment on the electrical properties (sheet resistance, electron mobility and electron density) and optical properties (transmission and absorption) of $\text{In}_2\text{O}_3:\text{H}$ films on glass is presented in Supplementary Fig. 3. The amorphous nature of the as-sputtered $\text{In}_2\text{O}_3:\text{H}$ is confirmed by X-ray diffraction (Supplementary Fig. 4). The radio-frequency sputtering method is a high-throughput and industrial scale method. However, high energetic ion bombardment during sputtering can damage the underlying layers. This is especially the case for organic layers such as Spiro-OMeTAD. Two different TCOs, that is, ZnO:Al and $\text{In}_2\text{O}_3:\text{H}$, are deposited by radio-frequency magnetron sputtering with different extent of ion bombardment and compared as transparent electrode.

The degree of ion bombardment is more severe during the deposition of ZnO:Al than that in $\text{In}_2\text{O}_3:\text{H}$ due to the different sputter geometries, lower total pressure and shorter target-to-substrate distance⁴⁸, as illustrated in Supplementary Fig. 5. In both devices, 8.7 nm MoO_3 is evaporated as buffer layer, and perovskite is grown from 120 nm-thick PbI_2 precursor. As can be seen in Fig. 3a,d, the average V_{oc} , J_{sc} , FF and η of devices with ZnO:Al are much lower than that of the ones with $\text{In}_2\text{O}_3:\text{H}$, and the s.d. is also larger in case of ZnO:Al. Notably, a perovskite solar cell with 10.1% efficiency (Supplementary Fig. 6) is achieved by directly depositing $\text{In}_2\text{O}_3:\text{H}$ on top of Spiro-OMeTAD. This is the

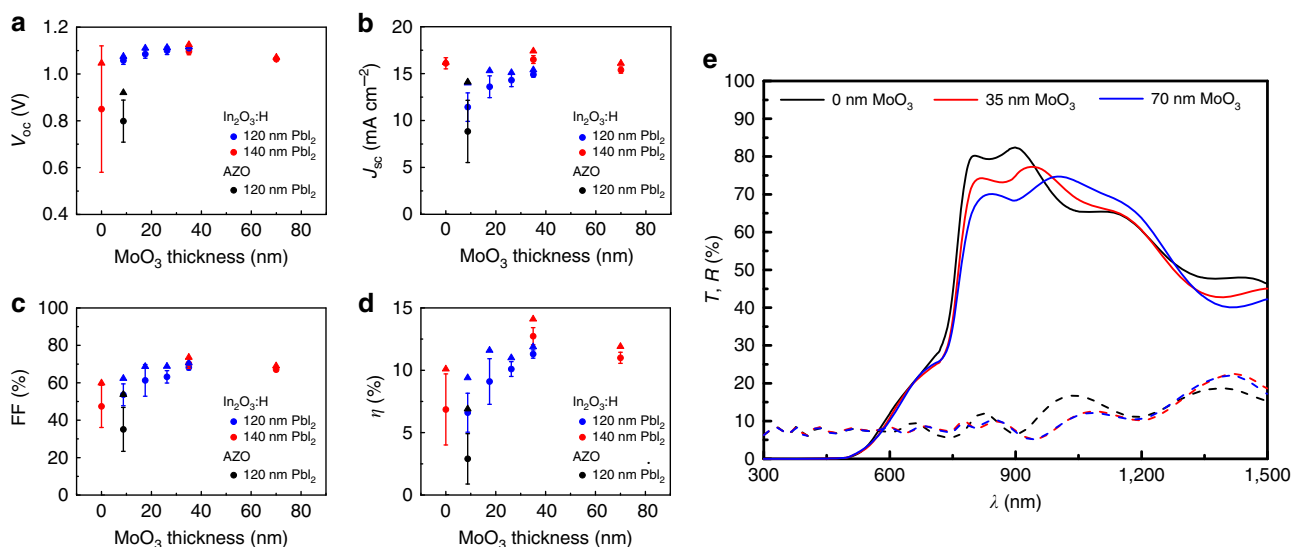


Figure 3 | Photovoltaic and optical properties of semi-transparent planar perovskite solar cells with different MoO₃ thickness. (a–d) The photovoltaic parameters of semi-transparent planar solar cells as a function of MoO₃ thickness with In₂O₃:H as rear transparent electrode. The photovoltaic performances of device with ZnO:Al rear contact are also presented for comparison. Average values and s.d. are given from 5 to 9 cells (cell area: 0.3 cm² for In₂O₃:H; and 0.15 cm² for ZnO:Al). The triangle symbol represents the highest value for each batch. The *J*-*V* measurement conditions were the same as in Fig. 2. (e) The transmission (*T*) and reflection (*R*) of semi-transparent cells with various MoO₃ thicknesses. The solid and dashed lines represent transmission and reflection, respectively. The perovskite is grown from 140 nm PbI₂ precursor. The MoO₃ thickness used here is determined from SEM images.

highest value with direct deposition of TCO on top of the hole transporting layer (HTL) as back electrode without buffer layer, indicating that direct sputtered TCO might allow to achieve high-efficiency if the ion bombardment is suppressed during deposition.

In the current device architecture and deposition procedure, the use of MoO₃ proves still to be beneficial. Figure 3 shows the photovoltaic and optical properties as a function of the MoO₃ thickness as well as the schematic cell structure of semi-transparent planar perovskite solar cell. A general increase of all the photovoltaic parameters combined with a substantial increase in uniformity is observed with increasing MoO₃ thickness up to 35 nm. Further, it is shown that the *J*_{sc} is less sensitive to MoO₃ thickness variation if the PbI₂ precursor thickness is increased to 140 nm while the FF and V_{oc} exhibit the same trend as devices grown from 120 nm PbI₂ precursors. For MoO₃ thicknesses above 35 nm no increase is observed anymore. The highest V_{oc} and FF in semi-transparent cells are comparable to opaque reference ones, indicating a reasonable trade-off between minimized sputtering damage and added series resistance with 35 nm MoO₃ thickness. In addition to the photovoltaic performance, the MoO₃ thickness also affects the transmission and reflection spectra as shown in Fig. 3e. The transmission shows a decreasing trend with increasing MoO₃ thickness between 800 and 940 nm, while an opposite trend with thickness variation between 940 and 1,200 nm. The device without MoO₃ shows a peak transmission of 82%, while device with 35 nm MoO₃ shows the highest average transmission in 800–1,150 nm region. Therefore, an optimal 35 nm-thick MoO₃ layer is deposit on Spiro-OMeTAD before In₂O₃:H deposition in terms of photovoltaic and optical properties in the following work.

Figure 4 summarizes the microstructure, transmission and photovoltaic performance of a semi-transparent planar perovskite solar cell produced as described above. The cross-sectional SEM image in Fig. 4a shows a cell structure of FTO/ZnO/PCBM/CH₃NH₃PbI₃/Spiro-OMeTAD/MoO₃/In₂O₃:H. An electron beam-evaporated Ni-Al grid is applied for better charge carrier

collection in cells with area above 0.5 cm². The cell area is defined by mechanical scribing down to the FTO layer. The perovskite grown from 140 nm PbI₂ and 45 mg ml⁻¹ CH₃NH₃I solution shows a flat and dense layer with grain size comparable to the film thickness. Figure 4b displays the transmission, reflection and absorption of the semi-transparent cell. The transmission through the whole device shows a peak of 77% at 940 nm and an average of 72% between 800 and 1,150 nm. The high sub-bandgap transmission is attributed to the low free-carrier absorption in high-mobility In₂O₃:H (ref. 48). In addition, the photograph of the semi-transparent device in the inset of Fig. 4b shows a decent transmission in visible region as the picture behind the device can be clearly recognized. The hatched area in Fig. 4b indicates optical losses due to insufficient absorption in the perovskite layer. This means there is still much room to increase the current in the semi-transparent cell by optimizing the (optical) thickness of perovskite layer.

Figure 4c,d presents the *J*-*V* curves and EQE spectra of the semi-transparent planar perovskite solar cell illuminated from front (FTO) and rear (In₂O₃:H) side. The forward and backward scans show negligible *J*-*V* hysteresis. The corresponding photovoltaic parameters are summarized in Supplementary Table 1. The semi-transparent device shows a V_{oc} of 1.104 V, *J*_{sc} of 17.4 mA cm⁻², FF of 73.6% and η of 14.1% illuminated from FTO, and V_{oc} of 1.105 V, *J*_{sc} of 12.2 mA cm⁻², FF of 70.6% and η of 9.5% illuminated from In₂O₃:H, as shown in Fig. 4c. The V_{oc} remains the same regardless of the illumination side, while higher *J*_{sc} and FF are observed when illuminated from FTO side. The EQE spectra are consistent with the *J*_{sc} discrepancy in *J*-*V* curves, where rear illumination shows a lower EQE, particularly below 430 nm. This distinct difference can be well explained by the strong parasitic absorption of Spiro-OMeTAD (Supplementary Fig. 7). Strong interference and the shading effect of metal grid also contribute to the lower current density when illuminated from rear side. The semi-transparent cell shows a high V_{oc} of 1.1 V, comparable to the reference cell. The FF is slightly reduced due to the lower conductivity of the In₂O₃:H/Ni-Al grid contact

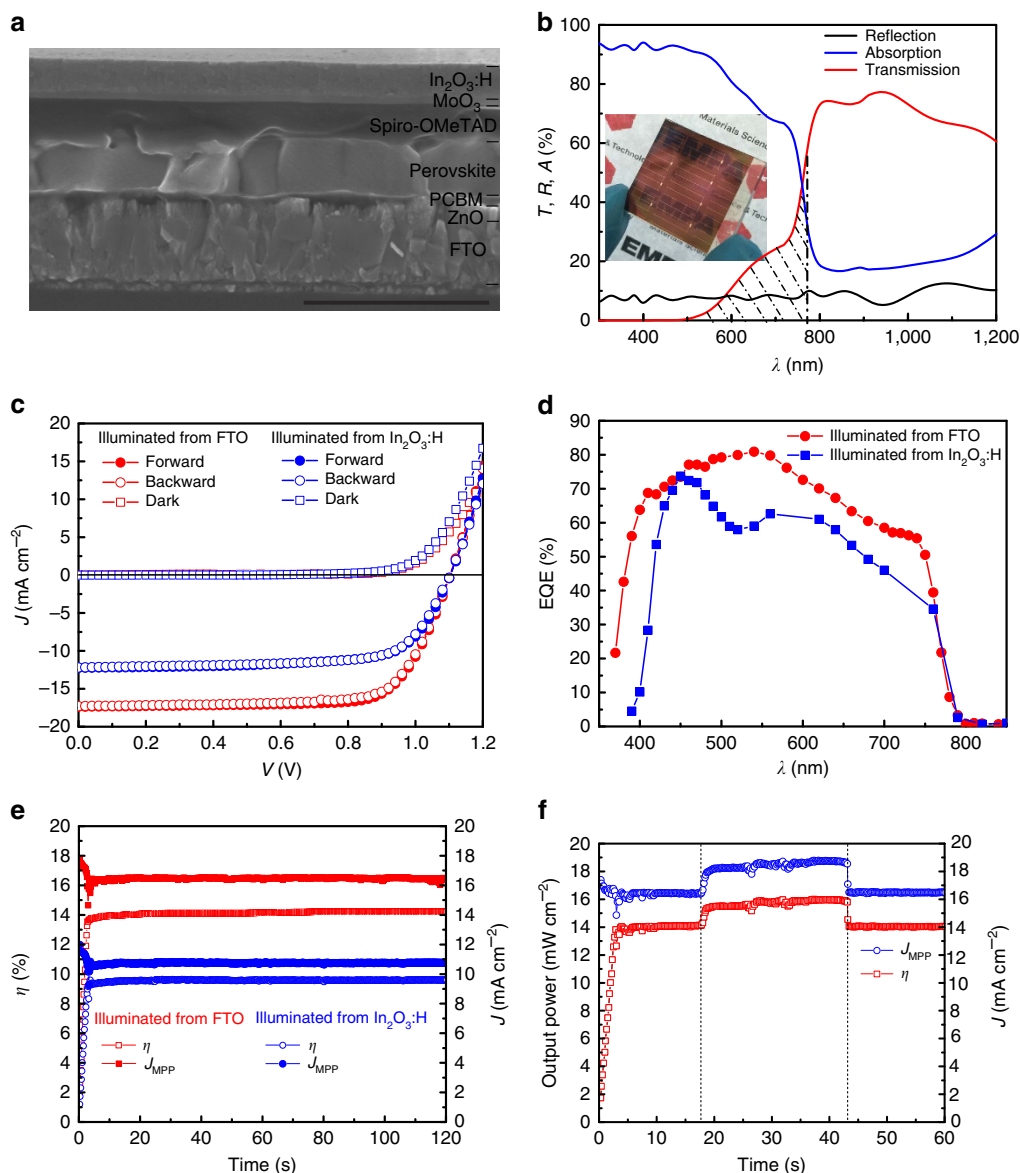


Figure 4 | Microstructure and photovoltaic performance of the semi-transparent planar perovskite solar cell. (a) The cross-sectional SEM image of the complete device. Scale bar, $1\mu\text{m}$. (b) The transmission (T), reflection (R) and absorption (A) of semi-transparent cell. A photograph of the semi-transparent device is also shown as inset. Current density-voltage (J - V) curve (c), external quantum efficiency (EQE) spectra (d) and steady-state efficiency at maximum power point (e) of the semi-transparent planar perovskite solar cell. (f) Bifacial application of the semi-transparent cell with white paper as reflective background. The first and second dashed lines indicate the insertion and removal of the commercial white paper as reflective background, respectively. The measurement conditions in the J - V , EQE and MPP are same as in Fig. 2.

compared with Au. Generally, the current density in the semi-transparent cell is lower than that in the opaque cell when the perovskite layer is grown from same PbI_2 thickness (120 nm) as shown in Supplementary Fig. 8. To verify the efficiency measured from J - V , the steady-state output at MPP is measured and presented in Fig. 4e. On illumination, the current density and efficiency increase within 3 s (ramp up of the MPP tracker) to 16.4 mA cm^{-2} and 14.2% for front illumination, and 10.8 mA cm^{-2} and 9.6% for rear illumination, respectively. The steady-state power conversion efficiency of 14.2% is the highest reported value for semi-transparent planar perovskite solar cell to date, which is particularly remarkable due to the simultaneously high transparency in NIR region. In addition, the semi-transparent cell with $\text{In}_2\text{O}_3\text{:H}$ showed improved air stability compared with the opaque cell with Au in a preliminary stability experiment, as shown in Supplementary Fig. 9. In the following,

two of many applications of high-efficiency semi-transparent perovskite solar cells are discussed in more detail.

Bifacial planar perovskite solar cell. Bifacial solar cells are capable of converting sunlight incident from the front and the rear side of the cell into electricity, therefore the power output could be improved if highly reflective surrounding is present behind rear side of the cell. To illustrate how the power output gain works, we simply put a white paper from a commercial notebook as reflective surrounding under rear side of the cell during the MPP measurement. As shown in Fig. 4f, the power output quickly increased from original 14.1 mW cm^{-2} after adding the white paper behind the solar cell, while it dropped back to 14.1 mW cm^{-2} after removing the white paper. Using white paper as reflective surrounding gives 13.5%

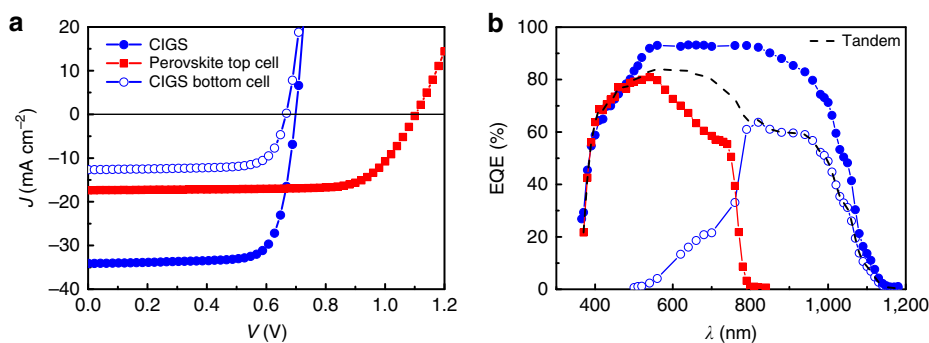


Figure 5 | Photovoltaic performance of the four-terminal perovskite-CIGS tandem solar cell. (a,b) The current density-voltage (J - V) curves (a) and EQE spectra (b) of the four-terminal tandem device.

Table 1 | Photovoltaic parameters of the four-terminal perovskite-CIGS tandem solar cells.

Solar cells	V_{oc} (mV)	J_{sc} (mA cm^{-2})	Calculated J_{sc} (mA cm^{-2})	FF (%)	η (%)	Steady-state efficiency (%)
Perovskite top subcell	1,104	17.4	16.7	73.6	14.1	14.2
CIGS cell (stand alone)	698.6	34.1	34.9	76.7	18.3	18.3
CIGS bottom subcell	667.4	12.7	12.4	74.9	6.3	6.3
Four-terminal tandem cell						20.5

performance enhancement. By using a more reflective background and proper arrangement of solar modules in a system, the output power gain can be further improved up to 50% as demonstrated in silicon technology by Ceuva *et al.*¹³.

Four-terminal perovskite-CIGS tandem solar cell. A four-terminal mechanically stacked tandem device is demonstrated based on perovskite as top subcell and CIGS as bottom subcell, as schematically shown in Supplementary Fig. 10. The CIGS absorber layer is fabricated by a multistage co-evaporation process⁴⁹. In a four-terminal tandem device, the top and bottom subcells are individually processed and mechanically stacked together. As the top cell and bottom subcell are electrically independent, two MPP trackers can be used to ensure optimum operation of each subcell at any condition. This also means that the efficiency of each subcell can be evaluated separately, and the sum of the two gives the efficiency of the device in tandem configuration. In this work, the performance of the bottom CIGS is directly measured with perovskite as a filter under standard illumination (Supplementary Fig. 10). The cell area of the bottom CIGS is defined by a laser-scribed shadow mask with aperture of 0.213 cm^2 inserted between the top and bottom subcells.

The J - V curves and EQE spectra of the top and bottom subcells are displayed in Fig. 5, and the photovoltaic parameters are summarized in Table 1. For comparison, the photovoltaic performance of the CIGS without perovskite filter is also presented. After adding the perovskite top cell as filter, the J_{sc} of the bottom CIGS decreased as expected due to reduced light intensity. The FF and V_{oc} are only marginally reduced, resulting in 6.3% efficiency for the CIGS bottom cell. Together with the 14.2% efficiency of the perovskite top, this result in 20.5% efficiency for the device in tandem configuration, which is a substantial improvement compared with each single-junction efficiency as well as to what was reported earlier for polycrystalline thin-film solar cells in tandem configuration^{32–35,50–52}.

Currently, the transmission is still limited by the strong parasitic absorption in the front FTO electrode. The low-temperature process presented here facilitates the use of more transparent TCOs, such as $\text{In}_2\text{O}_3:\text{H}$ or indium zinc oxide. The

transmission and absorption spectra of $\text{In}_2\text{O}_3:\text{H}$, $\text{ZnO}:\text{Al}$ and commercially available FTO and ITO are compared in Supplementary Fig. 11. The $\text{In}_2\text{O}_3:\text{H}$ has the lowest absorption among all the TCOs investigated here between 300 and 2,000 nm. This implies there is much room in further lowering the parasitic absorption of semi-transparent perovskite solar cell in NIR region if front FTO is replaced by high-mobility $\text{In}_2\text{O}_3:\text{H}$. Since both the fabrication process for the CIGS solar cell and the for the perovskite cell are compatible to deposition on polymer films, lightweight and bendable polycrystalline tandem devices are in reach. Optimization of the bandgap of top and bottom cells, application of anti-reflection coating and optical coupling media can lead to even higher tandem efficiency in the near future as discussed in more detail by Kranz *et al.*³³.

Discussion

In conclusion, a low-temperature-processed high-efficiency semi-transparent planar perovskite solar cell without J - V hysteresis is developed by using sputtered hydrogenated indium oxide ($\text{In}_2\text{O}_3:\text{H}$) as transparent rear electrode. The high-temperature-processed ($\sim 500^\circ\text{C}$) TiO_2 is replaced by room-temperature-sputtered ZnO , and the perovskite is prepared by a combined thermal evaporation of PbI_2 and spin coating of $\text{CH}_3\text{NH}_3\text{I}$ followed by 2-h annealing at 50°C , thus making the maximum processing temperature as low as 50°C . The hybrid thermal evaporation-spin coating method enables the introduction of PCBM in regular device configuration, which results in a high-quality perovskite layer and better electron collection, thus leads to a 14.5% hysteresis-free planar perovskite solar cell. High-mobility $\text{In}_2\text{O}_3:\text{H}$ is employed as transparent rear electrode deposited by sputtering at room temperature, which enables a semi-transparent planar perovskite solar cell with high steady-state efficiency of 14.2% and simultaneous 72% average transmission between 800 and 1,150 nm. Finally, we show a 13.5% output power enhancement when the semi-transparent cell functioned as bifacial solar cell and demonstrate 20.5% efficiency device with perovskite top cell and CIGS bottom cell in four-terminal tandem configuration. This work has significant beneficial implications in lightweight tandem solar cells, bifacial

solar cell, photon energy upconversion, photovoltaic-integrated buildings and wearable/portable electronics.

Methods

Perovskite solar cell fabrication. Perovskite solar cells were grown on FTO-coated glass (Pilkington, 15Ω per square.) substrates. The $5 \text{ cm} \times 5 \text{ cm}$ FTO/glasses were washed by hand followed by ultrasonic soap and water baths, and then cut into four quarters. Subsequently, a 100 nm compact ZnO layer was deposited at room temperature by radio-frequency magnetron sputtering on top of the FTO/glass at a deposition pressure of 6×10^{-3} mbar with Ar and O_2 flow of 45 and 16 sccm, respectively. The deposition power density was 1.9 W cm^{-2} , and the deposition time was 4.5 min. Then 30 μl of PCBM solution (20 mg ml^{-1} in chlorobenzene) was spin coated on top of ZnO at 2,000 r.p.m. for 40 s in the glovebox. The PbI_2 film was thermally evaporated on rotating PCBM/ZnO/FTO/glass substrates at a deposition pressure of $2\text{--}5 \times 10^{-8}$ mbar. Unless otherwise noted, the deposition rate is controlled within $1.2\text{--}1.6 \text{ \AA s}^{-1}$, monitored by a quartz crystal microbalance. The thicknesses of PbI_2 precursors for opaque cells is 120 nm. For semi-transparent devices, 120 and 140 nm were used. After the PbI_2 deposition, the samples were subsequently transferred into a N_2 -filled glovebox for further processing. The perovskite layer was formed by spin coating of $\text{CH}_3\text{NH}_3\text{I}$ (Dyesol, 99.9%) in 2-propanol at a concentration of 40 and 45 mg ml^{-1} for 120 and 140 nm PbI_2 , respectively. The solution was first spread to cover the whole substrate, and the rotation (2,000 r.p.m. for 40 s) was started after 10 s. The as-prepared films were annealed at $50 \text{ }^\circ\text{C}$ for 2 h on a hotplate inside the glovebox. After annealing, the samples were cooled down to room temperature and 30 μl of a Spiro-OMeTAD solution (72.3 mg 2,2',7,7'-tetrakis-(N,N' -di-*p*-methoxyphenylamine)-9,9'-spirobifluorene (Spiro-OMeTAD; Merck), 17.5 μl lithium-bis(trifluoromethanesulfonyl)imide (Li-TFSI, Sigma-Aldrich) solution (520 mg Li-TFSI in 1 ml acetonitrile, Sigma-Aldrich) and 28.8 μl 4-tertbutylpyridine (TBP, Sigma-Aldrich) all dissolved in 1,000 μl chlorobenzene (Sigma-Aldrich)) was spin coated on top of the perovskite at 2,000 r.p.m. for 40 s. The devices were finished by evaporating 60 nm Au through a metal mask under high vacuum ($< 5 \times 10^{-6}$ mbar), defining the cell area of 0.15 cm^2 for reference cells. For semi-transparent devices, a 35 nm thick MoO_3 was deposited on top of Spiro-OMeTAD via thermal evaporation, which was covered by 170 nm of $\text{In}_2\text{O}_3\text{:H}$ as transparent electrode. Ni/Al/Ni grids with 50 nm/2,000 nm/50 nm thickness were deposited by electron beam evaporation. Finally, the cell area (0.517 cm^2) is defined by mechanical scribing. No anti-reflection coating is applied for the semi-transparent cells.

Radio-frequency sputtering of hydrogenated indium oxide. Hydrogenated indium oxide ($\text{In}_2\text{O}_3\text{:H}$) layers were deposited in a high vacuum sputtering system (AJA Int.) by radio-frequency sputtering of ceramic In_2O_3 (99.99%) targets at an applied sputter power density of 3.0 W cm^{-2} without intentional heating of the substrate. The reactive atmosphere consisted of a gas mixture of Ar, O_2 and H_2O at a total pressure of 0.6 Pa. H_2O vapour for H doping was injected via a needle valve with a partial pressure of $\sim 1 \times 10^{-4}$ Pa.

Radio-frequency sputtering of aluminium doped zinc oxide. Aluminium-doped zinc oxide (ZnO:Al) layers were deposited in a high-vacuum sputtering system by radio-frequency sputtering of ceramic ZnO (containing 2 wt% Al_2O_3) targets. The sputtering deposition consist of a 5-min deposition ramp up from 0.6 to 2.5 W cm^{-2} and followed by $5 \times 3 \text{ min}$ at 2.5 W cm^{-2} under 20 sccm Ar and 0.29 sccm Ar/O_2 (3 mol% O_2). There is a 30-min waiting time during each step to alleviate the temperature effect.

X-ray diffraction measurements. X-ray diffraction patterns were obtained in Bragg–Brentano geometry by using a X'Pert PRO $\theta\text{--}2\theta$ scan (Cu- $\text{K}_{\alpha 1}$ radiation, $\lambda = 1.5406 \text{ \AA}$) from 10 to 60° (2θ) with a step interval of 0.0167° .

Scanning electron microscopy. The cross-sectional images of the samples were investigated with a Hitachi S-4800 using 5 kV voltage and 10 mA current. A thin layer of Pt was coated on top of the sample to avoid charging effect.

Ultraviolet-visible spectroscopy. The transmission (T) and reflection (R) spectra were acquired using a ultraviolet-visible-NIR spectrophotometer (Shimadzu UV-3600) equipped with an integrating sphere. Absorption A is calculated using the following formula: $A = 1 - T - R$.

Time-resolved photoluminescence. For time-resolved photoluminescence measurements, a 639 nm diode laser with pulse duration of 92 ps was used as excitation source. Pulse repetition rates were around 1 MHz and the number of photons per area and pulse was $\sim 1 \times 10^{13}$ photons per cm^2 . The spectrally integrated luminescence decay was measured using a Picoquant PMA-C 192-M photomultiplier time and a Picoquant TimeHarp 260 digitizing system with 50 ps time channel width.

Hall effect measurements. Hall effect measurements of $\text{In}_2\text{O}_3\text{:H}$ films were performed with a HMS 3,000 Hall effect measurement system at room temperature in the dark using van der Pauw geometry. The electron density and electron mobility were calculated from Hall measurements.

Solar cell performance characterization. The current density-voltage characteristics of perovskite solar cells were measured under standard simulated AM1.5G illumination using a Keithley 2,400 source meter. The illumination intensity was calibrated to $1,000 \text{ W m}^{-2}$ using a certified single crystalline silicon solar cell. The $J\text{--}V$ measurement is performed in both forward (from -0.1 V to 1.2 V) and backward (from 1.2 V to -0.1 V) directions separately without any pretreatment (for example, light soaking, holding at forward bias for certain time and so on). The scan rate and delay time are 0.3 V s^{-1} and 10 ms, respectively. The external quantum efficiency of the devices were measured with a lock-in amplifier. The probing beam was generated by a chopped white source (900 W, halogen lamp, 260 Hz) and a dual grating monochromator. The beam size was adjusted to ensure that the illumination area was fully inside the cell area. A certified single crystalline silicon solar cell was used as the reference cell. White light bias was applied during the measurement with ~ 0.1 sun intensity. The steady-state efficiency as a function of time was recorded using a maximum power point tracker, which adjusts the applied voltage in order to reach the maximum power point (perturb and observe algorithm). The starting voltage is set to be 0.1 V.

References

- Snaith, H. J. Perovskites: the emergence of a new era for low-cost, high-efficiency solar cells. *J. Phys. Chem. Lett.* **4**, 3623–3630 (2013).
- Stranks, S. D. & Snaith, H. J. Metal-halide perovskites for photovoltaic and light-emitting devices. *Nat. Nanotechnol.* **10**, 391–402 (2015).
- Yang, W. S. *et al.* High-performance photovoltaic perovskite layers fabricated through intramolecular exchange. *Science* **348**, 1234–1237 (2015).
- Beiley, Z. M. & McGehee, M. D. Modeling low cost hybrid tandem photovoltaics with the potential for efficiencies exceeding 20%. *Energy Environ. Sci.* **5**, 9173–9179 (2012).
- Hübner, A., Aberle, A. G. & Hezel, R. Novel cost-effective bifacial silicon solar cells with 19.4% front and 18.1% rear efficiency. *Appl. Phys. Lett.* **70**, 1008–1010 (1997).
- Cheng, Y. Y. *et al.* Improving the light-harvesting of amorphous silicon solar cells with photochemical upconversion. *Energy Environ. Sci.* **5**, 6953–6959 (2012).
- Hezel, R. Novel applications of bifacial solar cells. *Prog. Photovolt. Res. Appl.* **11**, 549–556 (2003).
- Zhou, C. Z. *et al.* in *Proceedings of the 26th IEEE Photovoltaics Specialists Conference* 287–290 (Anaheim, CA, USA, 1997).
- Schermer, J. J. *et al.* Photon confinement in high-efficiency, thin-film III-V solar cells obtained by epitaxial lift-off. *Thin Solid Films* **511**, 645–653 (2006).
- Nakada, T. *et al.* Novel device structure for Cu(In,Ga)Se_2 thin film solar cells using transparent conducting oxide back and front contacts. *Sol. Energy* **77**, 739–747 (2004).
- Khrypunov, G. *et al.* Recent developments in evaporated CdTe solar cells. *Sol. Energy Mater. Sol. Cell* **90**, 664–677 (2006).
- Ito, S. *et al.* Bifacial dye-sensitized solar cell based on an ionic liquid electrolyte. *Nat. Photon.* **2**, 693–698 (2008).
- Cuevas, A. *et al.* 50 percent more output power from an albedo-collecting flat panel using bifacial solar cells. *Sol. Energy* **29**, 419–420 (1982).
- Asadpour, R. *et al.* Bifacial Si heterojunction perovskite organic-inorganic tandem to produce highly efficient ($\eta_T \sim 33\%$) solar cell. *Appl. Phys. Lett.* **106**, 243902 (2015).
- Wang, J. *et al.* Photon energy upconversion through thermal radiation with the power efficiency reaching 16%. *Nat. Commun.* **5**, 5669 (2014).
- Cannavale, A. *et al.* Perovskite photovoltaic cells for building integration. *Energy Environ. Sci.* **8**, 1578–1584 (2015).
- Kim, B. J. *et al.* Highly efficient and bending durable perovskite solar cells: toward a wearable power source. *Energy Environ. Sci.* **8**, 916–921 (2015).
- Jeon, N. J. *et al.* Compositional engineering of perovskite materials for high-performance solar cells. *Nature* **517**, 476–480 (2015).
- Jeon, N. J. *et al.* Solvent engineering for high-performance inorganic-organic hybrid perovskite solar cells. *Nat. Mater.* **13**, 897–903 (2014).
- Burschka, J. *et al.* Sequential deposition as a route to high-performance perovskite-sensitized solar cells. *Nature* **499**, 316–319 (2013).
- Ahn, N. *et al.* Highly reproducible perovskite solar cells with average efficiency of 18.3% and best efficiency of 19.7% fabricated via Lewis base adduct of lead (II) iodide. *J. Am. Chem. Soc.* **137**, 8696–8699 (2015).
- Heo, J. H. *et al.* Hysteresis-less inverted $\text{CH}_3\text{NH}_3\text{PbI}_3$ planar perovskite hybrid solar cells with 18.1% power conversion efficiency. *Energy Environ. Sci.* **8**, 1602–1608 (2015).
- Zhou, H. *et al.* Interface engineering of highly efficient perovskite solar cells. *Science* **345**, 542–545 (2014).

24. Shao, Y. *et al.* Origin and elimination of photocurrent hysteresis by fullerene passivation in $\text{CH}_3\text{NH}_3\text{PbI}_3$ planar heterojunction solar cells. *Nat. Commun.* **5**, 5784 (2014).
25. Ryu, S. *et al.* Fabrication of metal-oxide-free $\text{CH}_3\text{NH}_3\text{PbI}_3$ perovskite solar cells processed at low temperature. *J. Mater. Chem. A* **3**, 3271–3275 (2015).
26. Xu, J. *et al.* Perovskite-fullerene hybrid materials suppress hysteresis in planar diodes. *Nat. Commun.* **6**, 7081 (2015).
27. Roldan-Carmona, C. *et al.* High efficiency single-junction semitransparent perovskite solar cells. *Energy Environ. Sci.* **7**, 2968–2973 (2014).
28. Zhen, L. *et al.* Laminated carbon nanotube networks for metal electrode-free efficient perovskite solar cells. *ACS Nano* **8**, 6797–6804 (2014).
29. Jiang, F. *et al.* Metal electrode-free perovskite solar cells with transfer-laminated conducting polymer electrode. *Opt. Express* **23**, 83–91 (2015).
30. You, P. *et al.* Efficient semitransparent perovskite solar cells with graphene electrodes. *Adv. Mater.* **27**, 3632–3638 (2015).
31. Snaith, H. J. *et al.* Anomalous hysteresis in perovskite solar cells. *J. Phys. Chem. Lett.* **5**, 1511–1515 (2015).
32. Loeper, P. *et al.* Organic-inorganic halide perovskite/crystalline silicon four-terminal tandem solar cells. *Phys. Chem. Chem. Phys.* **17**, 1619–1629 (2015).
33. Kranz, L. *et al.* High-efficiency polycrystalline thin film tandem solar cells. *J. Phys. Chem. Lett.* **6**, 2676–2681 (2015).
34. Wener, J. *et al.* Sputtered rear electrode with broadband transparency for perovskite solar cells. *Sol. Energy Mater. Sol. Cell* **141**, 407–413 (2015).
35. Bailie, C. D. *et al.* Semi-transparent perovskite solar cells for tandems with silicon and CIGS. *Energy Environ. Sci.* **8**, 956–963 (2015).
36. Guo, F. *et al.* High-performance semitransparent perovskite solar cells with solution-processed silver nanowires as top electrodes. *Nanoscale* **7**, 1642–1649 (2015).
37. Liu, D., Gangishetty, M. K. & Kelly, T. L. Effect of $\text{CH}_3\text{NH}_3\text{PbI}_3$ thickness on device efficiency in planar heterojunction perovskite solar cells. *J. Mater. Chem. A* **2**, 19873–19881 (2014).
38. Ke, W. *et al.* Efficient hole blocking layer-free planar halide perovskite thin-film solar cells. *Nat. Commun.* **6**, 6700 (2015).
39. Wu, Y. *et al.* Retarding the crystallization of PbI_2 for highly reproducible planar-structured perovskite solar cells via sequential deposition. *Energy Environ. Sci.* **7**, 2934–2938 (2014).
40. Chen, Y. *et al.* Layer-by-layer growth of $\text{CH}_3\text{NH}_3\text{PbI}_{3-x}\text{Cl}_x$ for highly efficient planar heterojunction perovskite solar cells. *Adv. Mater.* **27**, 1053–1059 (2015).
41. Fu, F. *et al.* Controlled growth of PbI_2 nanoplates for rapid preparation of $\text{CH}_3\text{NH}_3\text{PbI}_3$ in planar perovskite solar cells. *Phys. Status Solidi A* doi:1002/pssa.201532442 (2015).
42. Lee, Y. H. *et al.* Unraveling the reasons for efficiency loss in perovskite solar cells. *Adv. Energy Mater.* **25**, 3925–3933 (2015).
43. Lee, Y. H. *et al.* Controllable self-induced passivation of hybrid lead iodide perovskites toward high performance solar cells. *Nano Lett.* **14**, 4158–4163 (2014).
44. Maiberg, M. *et al.* Theoretical study of time-resolved luminescence in semiconductors. II. Pulsed excitation. *J. Appl. Phys.* **116**, 123711 (2014).
45. Metzger, W. K. *et al.* Analysis of charge separation dynamics in a semiconductor junction. *Phys. Rev. B* **71**, 035301 (2005).
46. Koida, T. *et al.* Hydrogen-doped In_2O_3 as high-mobility transparent conductive oxide. *Jpn J. Appl. Phys.* **46**, L685–L687 (2007).
47. Jäger, T. *et al.* Hydrogenated indium oxide window layers for high-efficiency $\text{Cu}(\text{In,Ga})\text{Se}_2$ solar cells. *J. Appl. Phys.* **117**, 205301 (2015).
48. Jäger, T. *et al.* Improved open-circuit voltage in $\text{Cu}(\text{In,Ga})\text{Se}_2$ solar cells with high work function transparent electrodes. *J. Appl. Phys.* **117**, 225303 (2015).
49. Chirila, A. *et al.* Highly efficient $\text{Cu}(\text{In,Ga})\text{Se}_2$ solar cells grown on flexible polymer films. *Nat. Mater.* **10**, 857–861 (2011).
50. Yang, Y. *et al.* Multilayer transparent top electrode for solution processed perovskite/ $\text{Cu}(\text{In, Ga})(\text{Se, S})_2$ four terminal tandem solar cell. *ACS Nano* **9**, 7714–7721 (2015).
51. Mailoa, J. *et al.* A 2-terminal perovskite/silicon multijunction solar cell enabled by a silicon tunnel junction. *Appl. Phys. Lett.* **106**, 121105 (2015).
52. Chen, C. *et al.* Perovskite/polymer monolithic hybrid tandem solar cells utilizing a low-temperature, full solution process. *Mater. Horiz.* **2**, 203–211 (2015).

Acknowledgements

Financial funding from Swiss National Science Foundation (SNF)-NRP70, PV2050 (project no.: 407040_153976 and 407040_153916), SNF-NanoTera and Swiss Federal Office of Energy (SYNERGY: 20NA21_150950), as well as Competence Center for Energy and Mobility (project CONNECT PV) are gratefully acknowledged. F.F. thanks the financial support from the Chinese Scholarship Council (CSC).

Author contributions

F.F., S.B. and A.N.T. designed the research and experiments; F.F., T.F., T.J. and A.E. fabricated the perovskite solar cells and CIGS solar cells; F.F., T.F., T.J., E.A., B.B., S.Y., S.B. and A.N.T. performed the characterization and analysis; F.F., S.B. and A.N.T. wrote the paper; all authors contributed to discussions.

Additional information

Supplementary Information accompanies this paper at <http://www.nature.com/naturecommunications>

Competing financial interests: The authors declare no competing financial interests.

Reprints and permission information is available online at <http://npg.nature.com/reprintsandpermissions/>

How to cite this article: Fu, F. *et al.* Low-temperature-processed efficient semi-transparent planar perovskite solar cells for bifacial and tandem applications. *Nat. Commun.* 6:8932 doi: 10.1038/ncomms9932 (2015).



This work is licensed under a Creative Commons Attribution 4.0 International License. The images or other third party material in this article are included in the article's Creative Commons license, unless indicated otherwise in the credit line; if the material is not included under the Creative Commons license, users will need to obtain permission from the license holder to reproduce the material. To view a copy of this license, visit <http://creativecommons.org/licenses/by/4.0/>